Journal of Materials Chemistry A

ROYAL SOCIETY OF CHEMISTRY

PAPER

View Article Online
View Journal | View Issue



Cite this: J. Mater. Chem. A, 2023, 11, 12202

# Enhanced sensitivity towards hydrogen by a TiN interlayer in Pd-decorated $SnO_2$ nanowires†

Clémence Badie, ‡[a] Jae-Hyoung Lee, ‡[b] Ali Mirzaei,[c] Hyoun Woo Kim,*[d] Syreina Sayegh, [e] Mikhael Bechelany, *[ef] Lionel Santinacci *[a] and Sang Sub Kim *[g]

In this study, we designed a new structure based on Pd-decorated TiN-coated $SnO_2$ nanowires (NWs) for the selective detection of $H_2$ gas. Initially, $SnO_2$ NWs were prepared by a simple vapor–liquid–solid growth method. Then, atomic layer deposition (ALD) was used to grow a continuous TiN layer and, subsequently, Pd nanoparticles on the NW networks. The TiN thickness was precisely set to 0.5, 1, 2, and 5 nm, while the Pd loading was adjusted by varying the number of ALD cycles (25 to 200 cycles). Various characterization techniques revealed the amorphous nature of TiN, a homogeneous dispersion of Pd NPs and the uniform morphology and single crystallinity of the $SnO_2$ NWs. $H_2$ gas sensing studies revealed that the sensor with a TiN thickness of 1 nm exhibited the highest response. Pd decoration further improved the response to $H_2$ gas. Hence, the Pd-decorated gas sensor with a 1 nm–thick TiN layer showed the highest $H_2$ sensing performance at 250 °C among all gas sensors. Due to the unique chemical reaction between Pd and hydrogen, the fabricated sensor shows excellent performance in detecting hydrogen gas. The underlying sensing mechanism is discussed in detail. The optimized sensor has a sensitivity of 8.18 for hydrogen gas, which is four times higher than that of other gas species, showing that it is suitable for detecting hydrogen gas. We believe that this new design is a highly valuable gas sensor for the real application of $H_2$ monitoring with high selectivity.

Received 2nd January 2023
Accepted 12th May 2023

DOI: 10.1039/d3ta00020f

rsc.li/materials-a



## 1 Introduction

Nowadays, due to high pollution and harms caused by the use of fossil resources, the development of sustainable and green energy is the general trend.[1] Hydrogen ($H_2$) is the most abundant element in the universe,[2] and its consumption does not generate toxic emissions.[3] It is, indeed, regarded as the most promising new fuel for vehicles.[4] Currently, it has many applications in different fields, such as biorefining, pharmaceuticals, metallurgy,[5] aerospace,[6] and automobile industry.[7]

However, its small kinetic diameter (0.289 nm) and high diffusion coefficient (0.61 $cm^2\ s^{-1}$) cause leakage from gas processing equipment.[8] Due to its flammable nature with a low explosive limit of 4.0 vol%, high heat of combustion, high flame propagation velocity, and low ignition energy, its leakage can lead to catastrophic accidents. In addition, its colorless and odorless nature makes it impossible to be perceived by human kinds,[9] and thus, it is important to develop highly efficient $H_2$ gas sensors capable of detecting very low concentrations to avoid dangerous accidents.[8,10,11] Furthermore, $H_2$ gas is a biomarker, and therefore, its presence in exhaled breath can be used for diagnosing some diseases,[12] such as small intestinal bacterial overgrowth, digestive disorders of dietary sugars (sucrose, fructose, lactose, and sorbitol), and normal food transport in the small intestine. Hence, the development of highly sensitive and selective $H_2$ gas sensors is important[13] not only from a safety point of view, but also from a medical standpoint.

There are many different types of gas sensors, such as work function,[12] electrochemical,[13] optical,[14] surface acoustic wave,[15] gasochromic,[16] colorimetric,[17] and electrical resistivity.[18] Among

[a]Aix Marseille Univ, CNRS, CINaM, Marseille, France. E-mail: lionel.santinacci@univ-amu.fr
[b]Electronic Materials Research Center, Korea Institute of Science and Technology, Seoul 02792, Republic of Korea
[c]Department of Materials Science and Engineering, Shiraz University of Technology, Shiraz 715557-13876, the Islamic Republic of Iran
[d]Division of Materials Science and Engineering, Hanyang University, Seoul 04763, Republic of Korea. E-mail: hyounwoo@hanyang.ac.kr
[e]Institut Européen des Membranes, IEM – UMR 5635, University of Montpellier, CNRS, ENSCM, Place Eugène Bataillon, Montpellier 34095, France. E-mail: mikhael.bechelany@umontpellier.fr
[f]Gulf University for Science and Technology, GUST, Kuwait
[g]Department of Materials Science and Engineering, Inha University, Incheon 22212, Republic of Korea. E-mail: sangsub@inha.ac.kr

† Electronic supplementary information (ESI) available: Schematic representation of the $SnO_2$ NWs synthesis. ALD mechanisms for TiN and Pd depositions. EDS analysis of the $SnO_2$ NWs after TiN and Pd depositions. *I–V* curves of composite materials. Transient resistance curves and response plots of synthesized materials. Response and recovery times of Pd/TiN (1 nm)/$SnO_2$ NWs. See DOI: https://doi.org/10.1039/d3ta00020f

‡ Co-first authors.

them, resistivity-based gas sensors are highly appreciated for gas sensing owing to their high response, high stability, fast dynamics, and low price.[19–21] In this type of gas sensors, the variations in resistance in the presence of the target gas is the basis of detection.[22] Many semiconducting metal oxides have been used for gas detection. Among them, $SnO_2$ is the most widely used for this purpose[23,24] because it exhibits many advantageous features for sensing applications, such as the high mobility of charge carriers, high stability, abundance and low price.[25–27] However, like other materials, such as ZnO and $WO_3$, $SnO_2$ gas sensors have no good selectivity especially in pristine form. Furthermore, they often need high operating temperatures to activate the sensor and to increase the number of charge carriers in the conduction band, which might be a drawback for some (not all) applications.

Since 1-dimension and morphology affect the sensing properties, $SnO_2$ nanostructures (*e.g.* wires, rods, belts, needles, whiskers, and sheets) have thus been implemented to improve the gas sensing properties such as, high surface area, fast response/recovery times and low power consumption.[28] In addition, for selectivity enhancement of $SnO_2$-based $H_2$ sensor devices, further strategies such as electron beam[29] or ion-beam irradiations,[30] heterojunction formation,[31] and noble metal functionalization[32,33] have been proposed so far.

Noble metals such as Pd, Pt, and Au have very high catalytic activities and they can reduce the gas adsorption energy and, hence, enhance the response and selectivity toward a specific gas at a lower sensing temperature. Furthermore, when the Fermi levels of noble metals are lower than the sensing layer, the energy bands of the sensing layer are bent at the interfaces, and the Schottky barriers will be formed due to the electron flow from the semiconductor to the noble metal. Changes in the height of the Schottky barrier in a $H_2$ atmosphere can significantly modify the resistance of the gas sensor, leading to the generation of an enhanced sensing signal.[34] Among different noble metals, Pd is particularly appropriated for $H_2$ detection.[35] Pd can easily dissociate adsorbed $H_2$ gas, converting it into atomic H, and then lead to a spillover effect, in which atomic species can be moved to the neighboring metal oxides and react with already adsorbed oxygen species. Furthermore, H atoms can diffuse into interstitial sites in the Pd lattice and convert it into $PdH_x$, exhibiting a higher resistance relative to metallic Pd. In addition, nanoparticles are more appropriate than continuous films due to the larger surface area developed. These effects can positively contribute to enhance $H_2$ selective sensing.[36] Finally, as mentioned by Yamazoe *et al.*[37] in contact with air, an electron depletion layer (EDL) is formed on the surface of sensing layers, due to partial oxidation of Pd into PdO. However, the EDL disappears when PdO is reduced into Pd in reducing atmospheres such as $H_2$ gas atmosphere. Accordingly, many researchers have used Pd for $H_2$ sensing enhancement.[38,39]

The combination of catalytic particles such as Pd or Pt with $SnO_2$ therefore appears to be one of the most efficient strategies. However, it has been shown that the catalytic activity of metallic particles can further be enhanced depending on the nature of the support. This improvement is known for a long time on oxidized supports for various processes.[40,41] For instance, oxides are still investigated as possible carbon support replacement in electrocatalysis (*e.g.* nanostructured $TiO_2$[42] or $SnO_2$ interlayer[43]), and a thin porous $Al_2O_3$ layer grown by molecular layer deposition (MLD) on $SnO_2$ nanowires (NWs) has been used as an efficient humidity sensor.[44] However, nitrides are now scrutinized with a strong interest. Recently, it has been shown that a BN interlayer enhances the sensing properties of supported Pd nanoparticles (NPs).[45] Transition metal nitrides have also been shown as possible replacement catalysts to Pt.[46] Among nitrides, TiN is very interesting since it is often used in microelectronics as a conductive layer[47–49] due to its stability at high temperatures and good ohmic contact (metal-like conductivity). It also prevents corrosion with good wear resistance.[50] Finally, TiN has been reported to be an efficient support for Pt minimization or replacement in the field of electrocatalysis[51] or photocatalysis.[52] Research on $H_2$ separation devices currently in progress in our groups reveals that TiN layer blocks the $H_2$ molecules while atomic H generated by Pd particles deposited on the TiN can cross it. Previous works have shown the sensing potential of $SnO_2$ nanowires (NWs).[44,53,54] Thus, the combination of a TiN thin layer as an interlayer between $SnO_2$ NWs and Pd NPs can be an efficient and novel strategy to enhance the overall $H_2$ gas sensing performance.

The target sensing system requires a compact and uniform TiN thin film as an interlayer to protect pristine $SnO_2$ underneath, allowing H atoms to diffuse through it. In addition, catalytic Pd NPs should be monodispersed on the overall 3D-$SnO_2$ NW network. No material accumulation or damage should occur during both TiN and Pd NP coatings to ensure that the high surface area of the $SnO_2$ NW network is maintained. Atomic layer deposition (ALD) is the method of choice to achieve such objectives while physical or chemical vapor deposition techniques exhibit coverage limitations.[55–58] Several examples cited above have already shown the interest of this deposition technique for such purpose (see, *e.g.* ref. 58 for review).

Initially, TiN films were mainly deposited using $TiCl_4$ associated with $NH_3$.[59] However, $TiCl_4$ requires high process temperatures and its by-products are corrosive. Then, organometallic precursors such as amides have become mostly used. Among them, tetrakis(dimethylamino)titanium (TDMAT)[60,61] is now predominant. TiN films exhibiting low carbon contamination, low roughness and low resistivity have already been conformally deposited using TDMAT and $NH_3$ onto different structured substrates such as nanoporous alumina and macroporous silicon.[62,63]

The ALD of Pd has been successfully performed on various substrates such as Ni, BN, and $TiO_2$.[42,43,64,65] Compared to TiN deposition, where both precursors, TDMAT and $NH_3$, are involved in the growth of the film, the Pd process deals with the reduction to metallic Pd and the elimination of the ligands of the Pd precursor by the co-reactant. In this case, after each cycle, metallic Pd atoms are deposited onto the substrate, forming nuclei. Then, in the following cycle, the deposition is more promoted to grow on the nuclei than on the substrate. This explains why metal particles, usually monocrystalline, are achieved instead of a compact film in the case of metals such as Pd,

Pt or Ru, as reported by Mackus *et al.*[66] and Ru by Federov *et al.*[67] In this work, Pd clusters are deposited by a direct ALD process, which uses palladium hexafluoroacetylacetone ($Pd(hfac)_2$) and formaldehyde, as previously described.[68–71]

According to the above-mentioned motivations, we report, for the first time, the fabrication process of a $H_2$ sensor device that involves coating $SnO_2$ NWs with a continuous ultra-thin TiN layer that is subsequently decorated with Pd NPs. $SnO_2$ NWs were synthesized by a simple vapor–liquid–solid (VLS) growth method. Both TiN and Pd depositions were performed by ALD with the possibility of exact control over the synthesis parameters. The gas sensing performance of bare $SnO_2$ NW, TiN/$SnO_2$ NW, Pd/$SnO_2$ NW and Pd/TiN/$SnO_2$ NW sensors was deeply studied. The results are discussed and they revealed that Pd/TiN/$SnO_2$ NW gas sensors have enhanced $H_2$ gas sensing performance in terms of sensitivity and selectivity in comparison with other $H_2$ gas sensors.

# 2 Experimental

## 2.1 Growth of $SnO_2$ NWs

$SnO_2$ NWs were fabricated by a VLS growth method. First, tri-layered Ti (50 nm), Pt (200 nm), and Au (5 nm) electrodes were fabricated in an interdigitated pattern by sputtering these metals onto an oxidized Si substrate ($SiO_2$ grown on Si). Then, the VLS method was used to grow networked $SnO_2$ NWs. Substrates with interdigitated electrodes were placed in a quartz tube furnace loaded with an $Al_2O_3$ crucible containing a metallic Sn powder (Aldrich, 99.9%). The furnace was heated to 950 °C for 1 h under the flow of Ar and $O_2$ gases simultaneously at rates of 300 and 10 sccm, respectively. Under these conditions, networked $SnO_2$ NWs grew selectively on the substrate. Fig. S1a† schematically illustrates the $SnO_2$ NW growth method.

## 2.2 ALD of TiN films

TiN deposition was performed on both $SnO_2$ NWs and HF (5%) cleaned Si(100) wafer pieces to monitor the thickness. TiN films were grown by thermal ALD in a shower-head geometry reactor Fiji 200 (Veeco/Cambridge Nanotech) according to the previous studies.[62,63] TDMAT (99.99%, Strem Chemicals) and $NH_3$ (≥99.999%, from Linde Electronics) were used as the Ti precursor and N-source, respectively, and Ar (≥99.999%, from Linde Electronics) served as the vector gas. TDMAT was maintained at 70 °C and the chamber temperature was fixed at $T_{TiN}$ = 200 °C. ALD sequences consist of pulsing, exposure and long purging successively TDMAT and $NH_3$ for defined durations (0.2 : 3 : 15 : 6 : 3 : 20 s). The thickness of the films ($t_{TiN}$) was adjusted by varying the number of ALD cycles ($N_{TiN}$) according to the growth per cycle of 1.1 Å/cycle (the surface reactions are schematically described in Fig. S2†).

## 2.3 ALD of Pd particles

Palladium NPs were deposited onto a $SnO_2$–TiN sensor in a home-built ALD reactor;[41,59,72] the deposition was performed at 220 °C using $Pd(hfac)_2$ (95% from Strem chemicals) heated at 70 °C and formalin (37% formaldehyde in water with 10–15% of methanol from Sigma-Aldrich) as the precursor and co-reactant, respectively. One cycle of ALD consisted of 5 s Pd pulse, 15 s exposure and 10 s Ar purge followed by 1 s pulse of $CH_2O$, 15 s exposure and 60 s Ar purge. A total of $N_{Pd}$ from 25 to 200 cycles was repeated to vary the desired Pd NP amount (the deposition mechanism is summarized in Fig. S3†).

## 2.4 Characterization methods

The TiN thickness was measured by *in situ* spectroscopic ellipsometry using a M2000V (J. A. Woollam Inc). Scanning and transmission electron microscopies (SEM and TEM) using a JSM 7900F (JEOL Ltd) and a JEM 2010 (JEOL Ltd), respectively, were performed to investigate the morphology of TiN films as well as the Pd NPs grown successively on $SnO_2$ NWs. Selected area electron diffraction (SAED) was performed in the TEM to locally study the crystal structure. The chemical composition was determined by energy-dispersive spectroscopy (EDS) using a Quantax FlatQuad (Bruker) and by X-ray photoelectron spectroscopy (XPS) using a Kratos Axis Ultra spectroscope (Kratos Analytical, UK) equipped with a monochromatic Al $K_\alpha$ source (1486.6 eV). The binding energy (BE) was corrected using the C 1s peak at 284.8 eV as an internal standard.

## 2.5 Sensor device fabrication

First, a Ti/Au bilayer electrode was deposited onto an alumina substrate. Then a paste was prepared by mixing the sensing powders with α-terpineol (20 μL) and then screen-printed on the sensor substrate (Fig. S1b†); subsequently, it was dried at 60 °C for 8 h.

## 2.6 Sensing measurements

The fabricated gas sensors were exposed to different gases at different temperatures using a specifically home-made designed sensing system (Fig. S1c†). The concentration of the target gas was precisely controlled by adjusting the mixing ratio between the target gas and dry air using accurate mass flow controllers (total flow rate = 500 sccm). During the sensing measurement process, the change in the resistance of the sensor in air ($R_a$) and in the presence of target gas ($R_g$) was continuously measured and recorded using a computer. The response was defined as $R = R_a/R_g$. The response and recovery times were defined as the time to reach 90% of the final resistance after exposure to the target gas and the time to recover 90% of the initial resistance of the sensor after removing the target gas, respectively. Details of gas sensing measurements can be found in.[73,74]

# 3 Results and discussions

## 3.1 Morphological and chemical studies

**3.1.1. General morphology of the sensing layer on the sensing device.** Fig. 1a presents an overall view of a typical sensing device, where the sensing layer is deposited on interdigitated electrodes. Fig. 1b shows the general morphology of the sensing layer ($SnO_2$ NWs) on the sensor and Fig. 1c is a high-

 

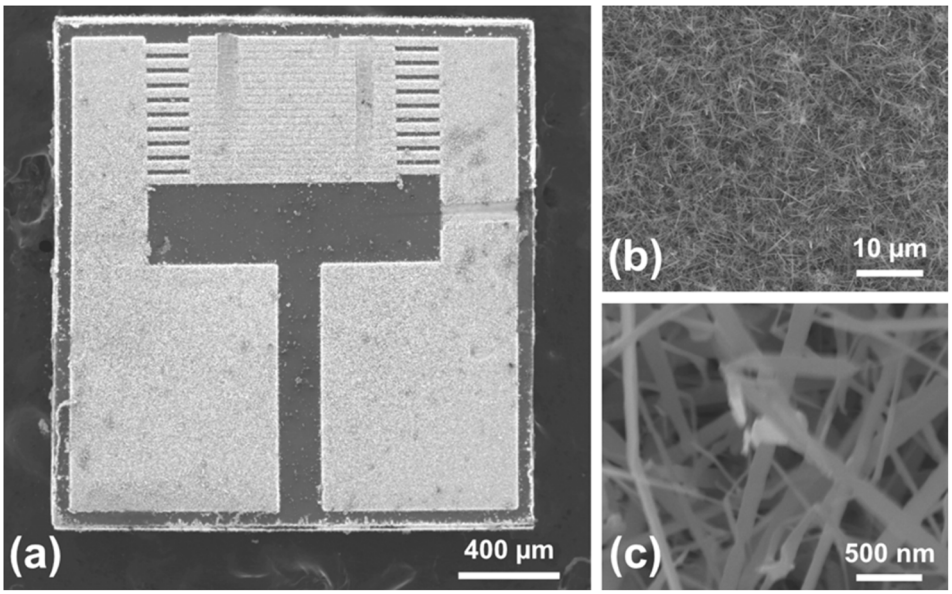


Fig. 1 SEM images of the bare sensor: (a) general view, and (b) and (c) $SnO_2$ NWs on the sensor substrate at two different magnifications.

resolution SEM image that reveals the expected morphology of the $SnO_2$ NW network. The synthesized $SnO_2$ NWs have a diameter ranging from 50 to 300 nm (mean diameter: ~80 nm) with a length in the order of ~5 μm. Accordingly, the aspect ratio of the $SnO_2$ NWs was calculated to be about 60.

**3.1.2. Morphological and structural studies of TiN.** Fig. 2a shows the typical TEM image of $SnO_2$ NWs covered by a 10 nm–thick TiN layer after $N_{TiN} = 100$ cycles. The coating is compact and the thickness ($t_{TiN} = 11 \pm 1$ nm) is constant on the whole NW. This demonstrates that the ALD process leads to uniform and conformal TiN deposition over a high aspect ratio (~60) of $SnO_2$ NWs. This is further confirmed by the high magnification observation shown in Fig. 2b. TiN indeed exhibits neither porosity nor columnar morphology and the $SnO_2$/TiN interface is sharp (*i.e.* while the (101) crystalline planes are visible in $SnO_2$, TiN looks mainly amorphous). This is expected from a previous work.[62] It is confirmed by the SAED pattern (inset in Fig. 2a) where only diffraction spots ascribed to single-crystalline $SnO_2$ are visible (according to PDF #00-41-1445). No additional spot or ring related to TiN was observed. Note that the observations on the 1 nm–thick TiN film did not lead to useable pictures because the layer was not easily distinguishable in the TEM. The interface with crystalline $SnO_2$ NWs underneath was not clear.

**3.1.3. Morphology and size studies of Pd NPs.** The deposition of Pd NPs on TiN-covered $SnO_2$ NWs was observed by TEM. Fig. 2c shows the general view of a NW, and the high magnification image of the tip after $N_{Pd} = 100$ cycles is shown in Fig. 2d. An uniform covering nature of the surface is observed. This is in agreement with Pd deposition performed earlier on BN.[65] The higher magnification image reveals the amorphous TiN thin layer at the NW tip (Fig. 2d). While it is known from the literature[42,43,65] that Pd particles are crystalline on various substrates (oxide or nitride), neither SAED nor XRD could properly demonstrate the crystallinity of the present Pd NPs. The moiré fringes observed on high-resolution TEM images (arrows on Fig. 2e) confirm, however, their crystallinity. Such fringes reflect, indeed, the superposition of two crystalline structures exhibiting different lattice parameters and a rotation, here, $SnO_2$ and Pd.[75] Fig. 2f shows the size distribution of Pd NPs, demonstrating that most of the NPs have a size of 6–7 nm.

**3.1.4. Chemical state study of Pd/TiN/$SnO_2$ NWs.** The surface composition of $SnO_2$ NWs covered by TiN and Pd has been investigated by XPS. In order to probe the full system, a sample exhibiting a thin TiN layer ($t_{TiN} = 1$ nm) has been selected. The analysis confirms the presence of all the elements constituting the device (Sn, Ti, Pd, O, and N) as well as the usual C 1s peak (see Fig. S4† for survey spectrum). Fig. 3 shows the main peaks of each element. The analysis of the Sn 3d area (Fig. 3a) indicates a predominant contribution attributed to the Sn–O bond in the $SnO_2$ matrix at BE = 487.1 eV (Sn $3d_{5/2}$) and BE = 495.7 eV (Sn $3d_{3/2}$) with a spin–orbit-splitting (SOS) of 8.5 eV. A minor contribution is also measured at BE = 485 eV (Sn $3d_{5/2}$) and BE = 493.6 eV (Sn $3d_{3/2}$). It is ascribed to unconverted metallic tin ($Sn^0$).[76] Ti 2p and N 1s peaks present very low intensities, which hinder precise fittings (Fig. 3b and e). These weak signals can be explained by the small relative sensitivity factors of these elements and the thinness of the film. The presence of Ti is also confirmed by energy-dispersive spectroscopy (EDS) analysis carried out during the SEM observations (Fig. S4†). Ti 2p peaks are relatively broad and positively shifted (Ti $2p_{3/2}$ is centered around 459 eV) but the expected SOS of 5.8 eV remains (Fig. 3b). According to earlier studies,[62,63] several contributions such as a nitride, oxynitride and oxide can be detected on the Ti 2p area, when TiN films are grown by this ALD process. Oxide and oxynitride contributions were ascribed to the oxidation of the top surface of the layer. Since the film is ultrathin, the top surface contributions, *i.e.* oxynitride and

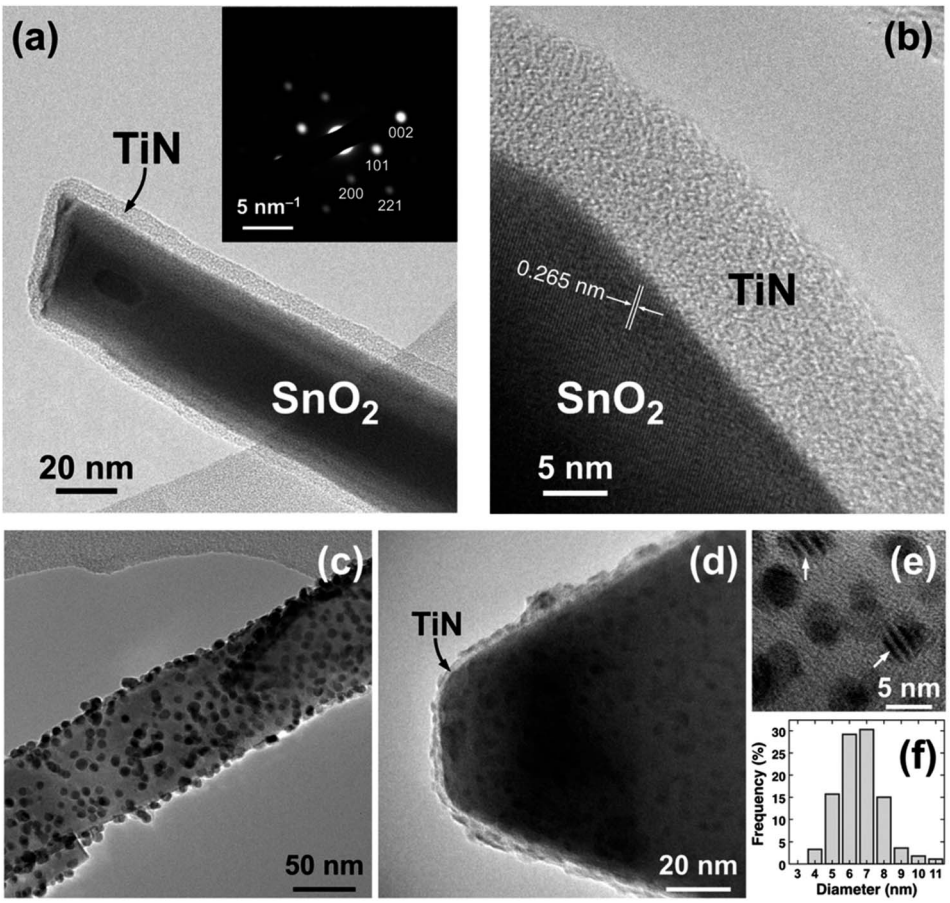


Fig. 2 (a) TEM image of a single $SnO_2$ NW after TiN deposition (inset shows the corresponding SAED image). (b) High-magnification TEM image of the $SnO_2$/TiN interface. TEM images of a single $SnO_2$ NW after TiN and Pd depositions: (c) general view of a $SnO_2$ NW and (d) focus on the tip of the $SnO_2$ NW. (e) High-resolution image of Pd NPs. (f) Size distribution histogram of the Pd NPs.

oxide, become predominant with regard to the bulk. Those Ti $2p_{3/2}$ components are usually expected at high energies (456.7 and 458.5 eV, respectively), while TiN is referenced at 455.3 eV.[77] The position of Ti $2p_{3/2}$ at BE = 459 eV could therefore question the presence of TiN. It is, though, supported by the detection of the broad N 1s peak near 400.2 eV (Fig. 3e). Again, the peak is positively shifted with regard to the expected N–Ti BE of 397 eV in TiN.[77] Since the signal-to-noise ratio is low, it is difficult to rigorously decompose the N 1s peak. It is possible to propose two components: one corresponding to N–Ti at low BE and another, at higher BE, ascribed to N–O. Those contributions should account for TiN and $TiO_xN_y$, respectively. The oxygen spectrum (Fig. 3d) exhibits a main peak at a lower energy (BE = 530.4 eV) corresponding to oxygen bonded to the metal, most likely ascribed to O–Sn in $SnO_2$ even if a tiny part should also be attributed to O–Ti related to the above-mentioned TiN oxidation. A shoulder centered at BE = 532.9 eV is attributed to oxygen bonded with carbon contaminations. The O–N component should appear around 531.4 eV[77] but $t_{TiN}$ is too thin to produce a significant signal. Pd $3d_{3/2}$ and $3d_{5/2}$ peaks located at BE = 341.0 and 335.5 eV, respectively (Fig. 3c), are sharp and show no shoulder. The doublet exhibits a SOS of 5.5 eV near the expected value of 5.25 eV. This demonstrates that $Pd^0$ NPs are deposited onto a thin composite film composed of TiN/$TiO_xN_y$/$TiO_2$. Finally, Fig. 3f shows the reference C 1s peak. As mentioned in the experimental section, C–C at BE = 284.8 eV is used as reference to calibrate all the spectra. A second contribution at a higher energy (BE = 286.6 eV) corresponds to the superficial contamination layer.

### 3.2 Electrical and gas sensing studies

Fig. S5† presents the *I–V* characteristics of Pd/TiN/$SnO_2$ NW gas sensors with different thicknesses of TiN layers (0.5, 1, 2, and 5 nm). In general, all gas sensors showed the Schottky contact between the sensing layer and electrodes. TiN tends to show an ohmic junction due to its unique conductivity, but in this study, it appears to be a Schottky junction due to the presence of $SnO_2$ and Pd.

In the first step and to find the optimal working temperature of gas sensors, we exposed the Pd/TiN (1 nm)/$SnO_2$ NW gas sensor to 1, 5 and 10 ppm $H_2$ gas at various temperatures, as shown in Fig. 4a. All gas sensors showed a n-type gas response originating from the n-type nature of $SnO_2$, where the resistance decreased in the presence of $H_2$ gas. The resistance is also modified depending on the working temperature from 150 to 350 °C. To have a better insight, the gas response was plotted

 

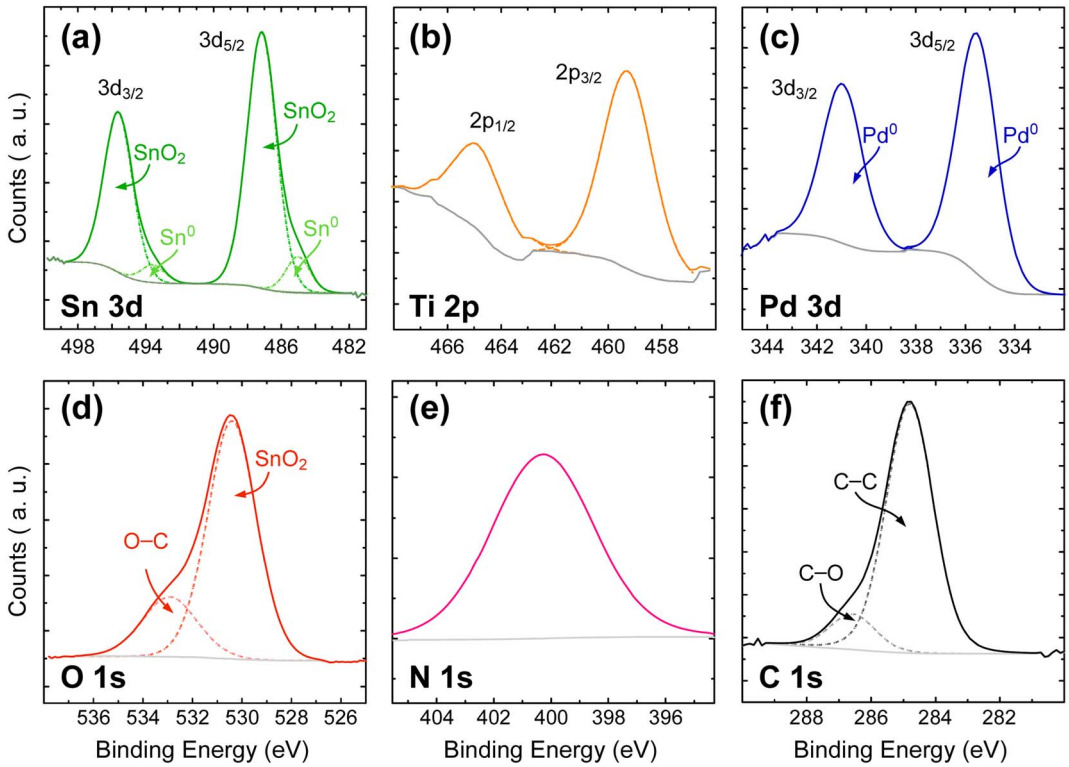


Fig. 3 XPS analysis of the $SnO_2$ NWs after successive ALD of TiN and Pd: (a) Sn 3d, (b) Ti 2p, (c) Pd 3d, (d) O 1s, (e) N 1s, and (f) C 1s peaks.

against the sensing temperature in Fig. 4b. It depicts the variations in the initial resistance of the gas sensor *versus* temperature where, as it was expected, the resistance decreased upon increasing the sensing temperature, reflecting the semiconducting nature of the sensing material. The sensor shows a bell-shaped behavior, where the response is low at temperatures <250 °C until showing a maximum at 250 °C and decreases again with further heating. Chemisorption occurs when bonds form between the adsorbate and the sensing layer by transferring electrons similar to the case of oxygen adsorption on the surface of gas sensors in which a monolayer of oxygen ions form on sensor surface.[78] At low operating temperatures, and due to the unavailability of electrons in the conduction band, physisorption is dominant and no significant electron transfer occurs between adsorbed oxygen species and sensing layer. However, at higher temperatures, more electrons jump to the conduction band of sensing materials, and hence, there are more available electrons to be abstracted by oxygen species. Therefore, at higher temperatures, it is expected that more chemisorbed oxygen species react with $H_2$ gas molecules and a higher response is expected. However, at very high temperatures, the desorption rate of both oxygen and target gas

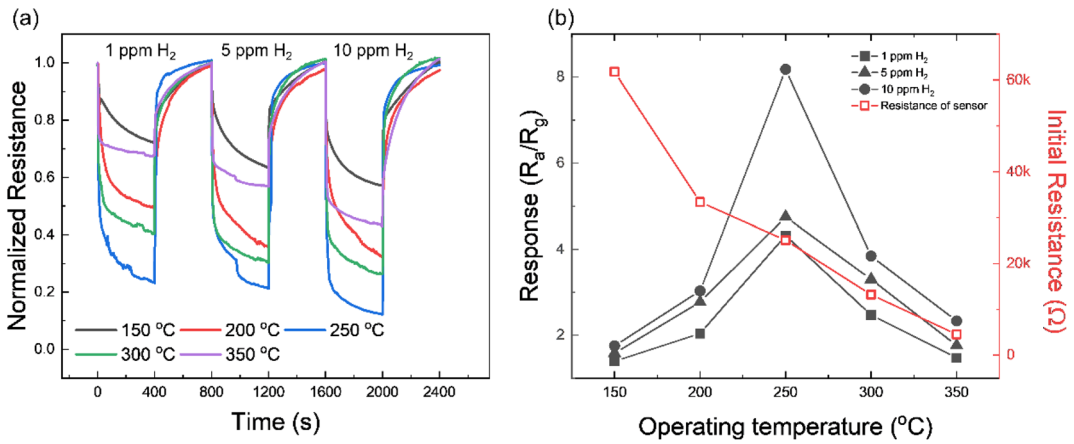


Fig. 4 (a) Dynamic resistance curves of the Pd/TiN (1 nm)/$SnO_2$ NW gas sensor to 1, 5 and 10 ppm $H_2$ gas at different temperatures. (b) Corresponding response as well as initial resistance *versus* operating temperature.

molecules is higher than the adsorption rate, leading to a further decrease in the gas response.[79] To assess the activation energy of oxygen chemisorption on the surface of materials, analysis of the kinetics of interaction between oxygen and the material is required. Hence the study of such mechanisms is really complex and should take into consideration several parameters which are beyond the scope of this work.[80,81] Moreover, sensors with different $t_{TiN}$ (Pd/TiN (0.5, 2, 5 nm)/$SnO_2$ NWs) were studied to find their optimal sensing temperature. Transient resistance curves and response/initial resistance *versus* temperature for Pd/TiN (0.5 nm)/$SnO_2$ NWs (Fig. S6a and b†), Pd/TiN (2 nm)/$SnO_2$ NWs (Fig. S6c and d†), and Pd/TiN (5 nm)/$SnO_2$ NWs (Fig. S6e and f†) were obtained. The optimized sensing temperatures were 200, 250 and 300 °C for the sensor with 0.5, 2 and 5 nm–thick TiN layers, respectively. The response of these gas sensors at their optimal working temperatures was lower than that of the Pd/TiN (1 nm)/$SnO_2$ gas sensor at its optimal sensing temperature (250 °C). Therefore, other sensing studies were performed at 250 °C.

In the next step, TiN/$SnO_2$ NW gas sensors with 1, 2 and 5 nm TiN thicknesses were exposed to 1, 5 and 10 ppm of $H_2$ gas at 250 °C. Fig. 5a shows the dynamic resistance curves and Fig. 5b the corresponding response *versus* $t_{TiN}$. For all tested concentrations, the response of the sensor with a 1 nm–thick TiN layer is higher than that of other gas sensors, demonstrating, therefore, that it is the optimal thickness. Variations in the initial sensor resistance are depicted. Sensor with the thickest TiN layer showed the highest initial resistance. TiN is known as a conductive material, but in this study, resistance tends to increase with the increase in thickness. This seems to be due to the influence of very small amounts of $TiO_2$ and $TiO_xN_y$ shown in the XPS data of Fig. 3. The above-mentioned experiments were repeated for Pd/TiN (0.5, 1, 2, and 5 nm)/$SnO_2$ NW gas sensors, and the results are presented in Fig. 5c and d. The sensor with a TiN layer with a thickness of 1 nm showed the highest response to $H_2$ gas for all concentrations.

To study the effect of Pd NPs, the $H_2$ gas sensing tests were performed by controlling the number of deposition cycles from 25 to 200 to make Pd (25, 50, 100, and 200 cycles)/TiN (1 nm)/$SnO_2$ NW gas sensors. Fig. S7a† gives the dynamic resistance curves of different gas sensors with various Pd NP cycles. Based on Fig. S7b,† since the response of the sensor with 100 cycles of Pd was higher than the response of other gas sensors, remaining tests were performed using the sensor with 100 cycles of Pd deposition.

We also tested the responses of pristine $SnO_2$ NWs and Pd/$SnO_2$ NWs to 1–10 ppm of $H_2$ gas at 250 °C, as shown in Fig. S8a and b,† respectively. To better understand the performance of different gas sensors, their response to 1, 5 and 10 ppm $H_2$ gas is summarized in Fig. S9.† Based on these data, the (100 cycles)Pd/TiN (1 nm)/$SnO_2$ NW gas sensor showed the optimal gas sensing results in this study.

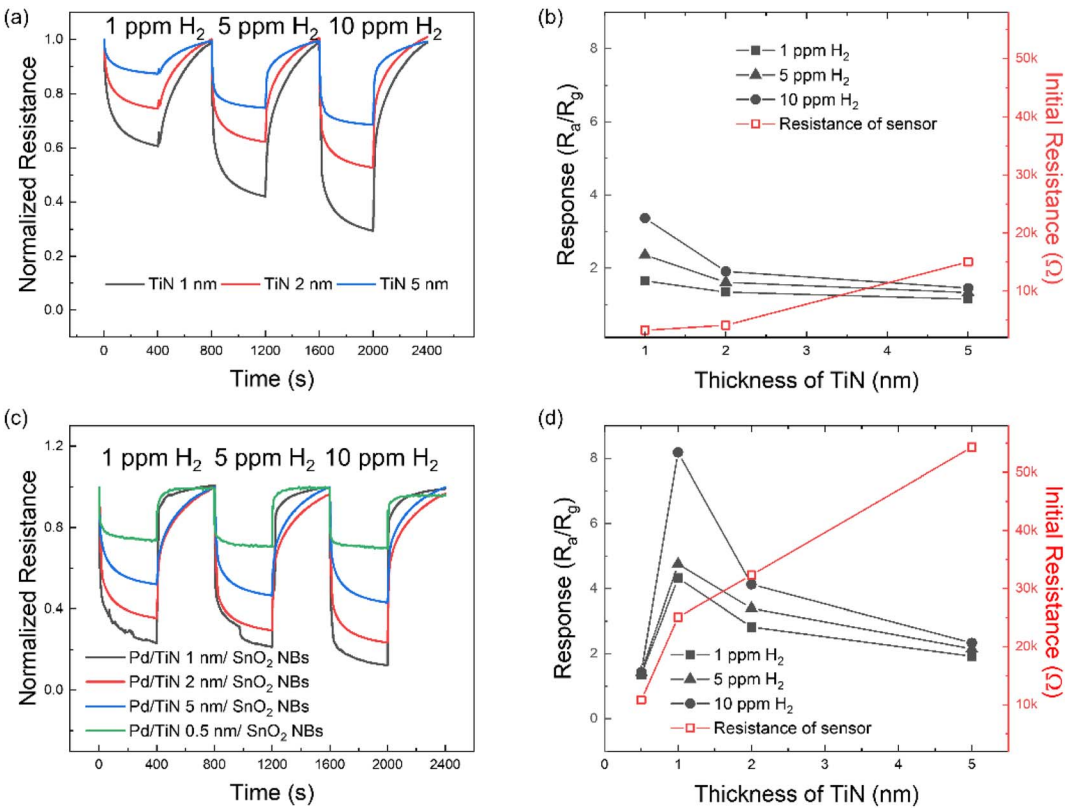


Fig. 5 (a) Dynamic resistance curves of TiN (1, 2, and 5 nm)/$SnO_2$ NW gas sensors to 1, 5 and 10 ppm $H_2$ gas at 250 °C. (b) Corresponding response and initial resistance *versus* thickness of the TiN layer. (c) Dynamic resistance curves of Pd/TiN (0.5, 1, 2, and 5 nm)/Pd/$SnO_2$ NW gas sensor to 1, 5 and 10 ppm $H_2$ gas at 250 °C. (d) Corresponding response and initial resistance *versus* thickness of the TiN layer.

 

Since selectivity is of importance for practical applications, we also measured transient resistance curves of optimal gas sensors by exposing it to 1, 5 and 10 ppm of various gases ($H_2$, CO, $C_6H_6$, $C_7H_8$ and $NH_3$) as shown in Fig. 6a. The corresponding responses to different gases are plotted in Fig. 6b. Obviously, the response to $H_2$ gas is higher than that for other gases, reflecting the high $H_2$-sensing selectivity of the optimized gas sensor. Moreover, Fig. S10† shows the response and recovery times of Pd/TiN (1 nm)/$SnO_2$ NW gas sensors to 10 ppm of various gases. Both response and recovery times were shorter than other tested gases, confirming that the as-fabricated gas sensor could detect $H_2$ gas molecules faster than other gases.

Fig. S11a† offers the dynamic resistance curves of Pd/TiN (1 nm)/$SnO_2$ NW gas sensors to 10 ppm $H_2$ gas in the presence of different relative humidity (RH) levels (from 20 to 60%), and corresponding response *versus* RH (%) are presented in Fig. S11b.† Increasing RH from 20 to 60%, the response of the gas sensor decreased from 6.63 to 4.56. When water vapor is present in the environment, water molecules adsorb onto the surface of the sensing layer and occupy some adsorption sites. Hence, the number of available sites for incoming $H_2$ gas molecules decreases. Therefore, reduced amounts of $H_2$ gas can be adsorbed onto the surface, resulting in a lower response in the presence of humidity. Fig. S12a† shows the dynamic resistance curves of Pd/TiN (1 nm)/$SnO_2$ NW gas sensors to 10 ppm $H_2$ gas after two years, and Fig. S12b† shows the corresponding response *versus* the cycle number. Moreover, for comparison, the response of the fresh gas sensor is shown. The fresh sensor shows a response of 8.18 to 10 ppm $H_2$ gas, and after two years, the response during different cycles was varied between 7 and 8.66, reflecting the good stability of the optimized gas sensor even after two years.

To explore the experimental detection limit, the optimal gas sensor was exposed to various $H_2$ concentrations (0.1–50 ppm), and the corresponding results are shown in Fig. S13a and b.† As presented in results, the fabricated gas sensor detects very low concentrations of hydrogen gas. Therefore, the present sensor successfully detected the very low concentrations of $H_2$ gas. Then, the detected concentrations of $H_2$ gas are much lower than the explosive limit of $H_2$ gas. Hence, the present optimal gas sensor can reliably detect very low concentrations of $H_2$ leakages in real applications and prevent the explosions caused by $H_2$ leakage as the explosion limit of $H_2$ gas is 4%.

The response of the Pd/TiN (1 nm)/$SnO_2$ NW sensor is compared with those reported in the literature, as summarized in Table 1. In a comparative view, it can be deduced that the gas sensor fabricated in this study exhibited the excellent hydrogen detection properties, in terms of operating temperature as well as response. In particular based on the sensitivity factor which is defined as "response/concentration", the present sensor shows much enhanced performance relative to other gas sensors listed in Table 1.

### 3.3 Gas sensing mechanism

Fig. 7a illustrates the various sensing materials, namely, $SnO_2$ NWs, TiN/$SnO_2$ NWs and Pd/TiN/$SnO_2$ NWs grown on the interdigitated pattern, and herein, we will discuss the sensing mechanisms of different sensing materials. Initially, in air, oxygen molecules adsorb onto the surface of the sensing layer, taking electrons due to their high electron affinity. The relevant reactions can be shown as follows:[22]

$$O_2(g) \rightarrow O_2(ads) \quad (1)$$

$$O_2(ads) + e^- \rightarrow O_2^-(ads) \quad (2)$$

$$O_2^-(ads) + e^- \rightarrow 2O^- \quad (3)$$

$$O^- + e^- \rightarrow O^{2-} \quad (4)$$

It should be noted that each oxygen ionic species is stable in the temperature range. For example, at high temperatures (>300 °C), $O^{2-}$ species are dominant.[88] Therefore, in this study, dominant species are $O^-$ ions because the working temperature is set to 250 °C.

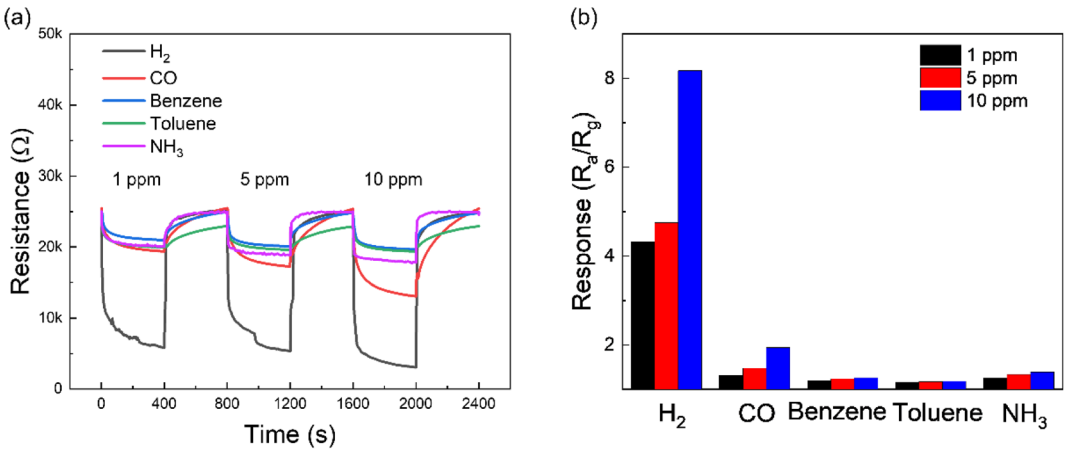


Fig. 6 (a) Dynamic resistance curves of Pd/TiN (1 nm)/$SnO_2$ NW gas sensors to various concentrations of $H_2$, CO, benzene, toluene, and $NH_3$ in concentrations 1, 5, and 10 ppm in the mixture with air at 250 °C. (b) Corresponding response to different gases.

Table 1 Hydrogen sensing performance of the Pd/TiN (1 nm)/$SnO_2$ NW gas sensor reported in this study compared with those reported in the literature

| Sensor | Conc. (ppm) | Temp. (°C) | Response | Sensitivity factor | Ref. |
|---|---|---|---|---|---|
| Pd/TiN (1 nm)/$SnO_2$ NWs | 10 | 250 | 8.18[a] | 0.818 | This study |
| $SnO_2$ NWs | 10 | 250 | 2.72[a] | 0.272 | 82 |
| Pd-$SnO_2$ NWs | 10 | 400 | ~2.5[a] | 0.250 | 83 |
| $SnO_2$ thin film sensitized with microsized Pd islands | 100 | 300 | ~2[a] | 0.020 | 81 |
| 2D $SnO_2$ disks | 100 | 350 | ~6.5[a] | 0.065 | 84 |
| Pd/$SnS_2$/$SnO_2$ | 500 | 300 | ~7.5[a] | 0.015 | 8 |
| $SnO_2$-$Cr_2O_3$ | 400 | 250 | ~30%[b] | 0.075 | 85 |
| $SnO_2$ NSs | 50 | 300 | 3.2[a] | 0.064 | 86 |
| Pd doped rGO/ZnO–$SnO_2$ | 100 | 300 | ~4.5[a] | 0.045 | 87 |

[a] $R_a/R_g$. [b] $\Delta R/R_0 \times 100\%$.

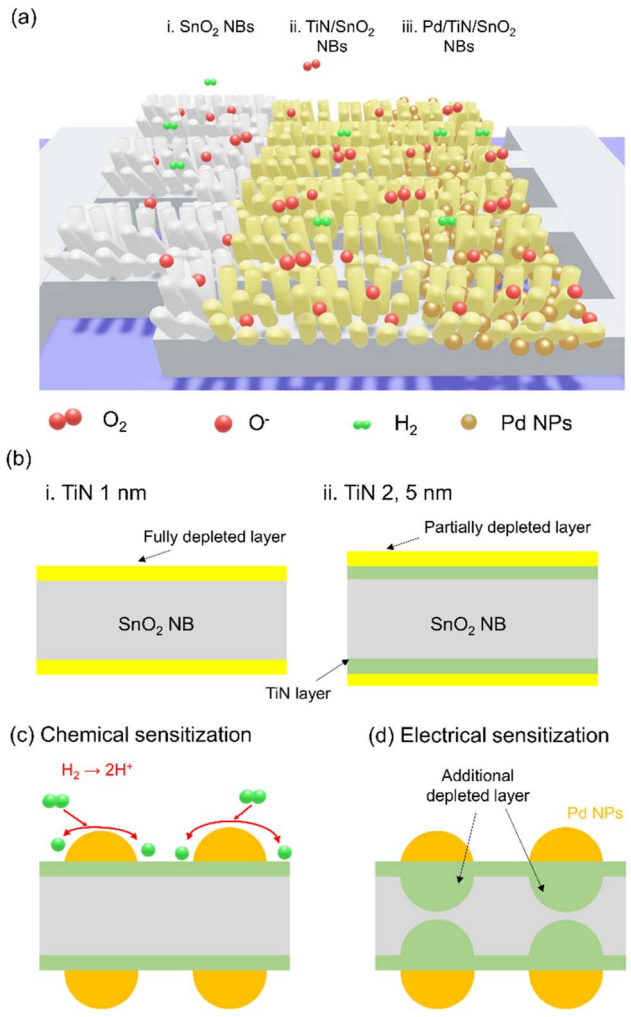


Fig. 7 Schematic images of (a) as-grown $SnO_2$ NWs, TiN/$SnO_2$ NWs and Pd/TiN/$SnO_2$ NWs, (b) role of TiN interlayer with different thicknesses, (c) electrical sensitization and (d) chemical sensitization of Pd NPs.

As a result, the so-called EDL will be formed on the $SnO_2$ NW surface, limiting the conductivity to inner parts on the $SnO_2$ NW, named conduction channels in the following. In air, the diameter of the conduction channels is smaller than when the sensor is in a pure $N_2$ gas atmosphere, where there is no adsorbed oxygen. By subsequent exposure to $H_2$ gas, the following reaction can take place:[89]

$$H_2 + O^- \rightarrow H_2O + e^- \quad (5)$$

According to the above-mentioned reaction, electrons are released upon reaction between $H_2$ and adsorbed oxygen species. This leads to narrowing the EDL and increasing the diameter of the conduction channel inside of $SnO_2$ NWs. This ultimately leads to a decrease in the resistance, as observed in dynamic resistance curves. Furthermore, due to the networked nature of $SnO_2$ NWs, many contact areas and potential barriers can be created at $SnO_2$–$SnO_2$ homojunctions in air. Upon exposure to $H_2$ gas, the height of the potential barrier decreases, and a remarkable modulation in the resistance of the sensor occurs.[90]

Fig. S14† depicts the band diagram of Pd/TiN/$SnO_2$ upon intimate contact. The work function of $SnO_2$ (4.55 eV)[91] is lower than that of Pd (5.6 eV) and TiN (4.65 eV).[92] Thus, electrons flow from $SnO_2$ to Pd and TiN, creating a Schottky junction with a potential barrier to electron flow in air. As a result, the electron depletion layer will appear inside $SnO_2$ in interfaces between $SnO_2$/Pd and $SnO_2$/TiN. Upon exposure to $H_2$ gas, the height of the formed junctions decreases, leading to the narrowing of electron depletion layers inside $SnO_2$, and eventually decreases the sensor resistance.

Furthermore, since some parts of the TiN film are exposed to air in TiN-coated and Pd-NPs-TiN-coated $SnO_2$ NW sensors, these areas will also be depleted from electrons by adsorbed oxygen ions. Accordingly, in a $H_2$ gas atmosphere and by releasing back of electrons, more modulation of the resistance is expected. It was found that the sensor with a TiN layer thickness of 1 nm showed the highest response to $H_2$ gas. Indeed, we should consider two factors that contribute to the sensing signal. The first one is the thickness of the TiN layer and the second one is the total thickness of the $SnO_2$ + TiN layer. For the sensor with the thinnest layer of TiN (0.5 nm), even though

 

the whole TiN layer may be depleted from electrons in air (Fig. 7b), that thickness is much smaller than the overall $SnO_2$ + TiN thickness and upon exposure to $H_2$ gas, the resistance modulation is not significant and the response value is lower than that of the sensor with a thicker TiN layer. Moreover, for the sensors with a TiN layer thicker than 1 nm, the overall thickness of TiN is not depleted from the electrons and upon exposure to $H_2$ gas, no significant modulation of resistance occurs again. However, for the sensor with a TiN layer of 1 nm, it seems that not only the whole thickness of TiN become depleted from electrons, but also the ratio of TiN thickness to overall $SnO_2$ + TiN thickness is noticeable. Hence, upon exposure to $H_2$ gas, a large modulation of the electrical resistance occurs, resulting in a higher response for the sensor with a TiN layer of 1 nm.

Pd decoration led to a higher response of $H_2$ gas sensors. As shown in TEM images (Fig. 2), Pd NPs are dispersed on the surface of $SnO_2$ NWs. Hence, the gas response significantly increases by the catalytic activity of Pd on $H_2$. In the $H_2$ gas ambient, Pd facilitates the dissociation of molecular $H_2$ into H atoms (Fig. 7c), which migrate to the TiN surface by the so-called spillover mechanism. H atoms then react with the adsorbed oxygen ions on the TiN surface and the electrons are returned back to $SnO_2$. The relevant reactions are as follows:[93]

$$H_2 \rightarrow H + H \quad (6)$$

$$H \rightarrow H^+ + e^- \quad (7)$$

$$2H^+(ads) \xrightarrow{O^{2-}(ads)} H_2 \quad (8)$$

The above-mentioned reactions lead to a significant decrease in resistance, yielding to a high response. The modulation of the resistance in the TiN/Pd heterojunction also contributes to the evolution in the sensing activity of the gas sensor. Due to the work function difference of materials as mentioned above, the electron-depletion regions are generated in TiN, and a subsequent exposure to $H_2$ gas, will result in a greater resistance modulation (Fig. 7d). Moreover, the $H_2$ gas can be directly dissolved in octahedral sites of Pd, changing its metallic state ($Pd^0$) into a hybrid form ($PdH_x$), which ultimately will affect the overall resistance of the gas sensor. The formation of $PdH_x$ was confirmed in a recent study by our group using XPS studies.[94]

In addition to the promising catalytic role of Pd towards $H_2$ gas, the selectivity of the optimized $H_2$ gas sensor can be related to the small kinetic diameter of the $H_2$ gas molecule (2.89 Å), relative to $C_6H_6$ (5.85 Å), CO and $C_7H_8$ (5.8 Å) molecules. Accordingly, $H_2$ gas molecules can more easily penetrate the $SnO_2$ NW gas sensor structure, resulting in a higher gas response.[94]

# 4 Conclusions

In brief, we introduced a novel gas sensor based on Pd-decorated TiN-coated $SnO_2$ NWs. TiN with thicknesses of 0.5, 1, 2 and 5 nm was deposited over a $SnO_2$ NW network, followed by Pd decoration with different amounts depending on the number of cycles applied (from 25 to 200 cycles). ALD was used to conformally deposit TiN and uniformly distribute Pd NPs. Based on the characterization results, amorphous TiN films were conformally coating the $SnO_2$ NWs, as well as the crystalline Pd NPs were homogeneously dispersed over TiN. $H_2$ gas sensing results indicated that the sensor with 100 cycles-Pd decoration and a 1 nm–thick TiN layer had the highest response to $H_2$ gas. Enhanced gas response and high $H_2$ sensing selectivity were related to different causes: the catalytic effect of Pd towards $H_2$ gas, small kinetic diameter of $H_2$ gas, high surface area of $SnO_2$ NWs, formation of $SnO_2$/TiN heterojunctions as well as Pd/TiN heterojunctions. Successful results obtained in this study can be extended to other similar systems to improve the overall gas sensing performance.

# Conflicts of interest

There are no conflicts to declare.

# Acknowledgements

The authors acknowledge D. Chaudanson and A. Altié (CINaM) for their valuable help with the electron microscopy. This collaborative work was supported by the French Agence Nationale de la Recherche (ANR) under grant ANR-17-CE09-0049-03 (project MENINA). Sang Sub Kim also acknowledges the support from the Korea Polar Research Institute (KOPRI) grant funded by the Ministry of Oceans and Fisheries (KOPRI project No. PE22900), and a National Research Foundation of Korea (NRF) grant funded by the Korean government (MSIT) [No. 2021R1A2C1009790].

# References

1 Z. Shi, J. Feng and X. Dong, *Int. J. Hydrogen Energy*, 2022, DOI: 10.1016/j.ijhydene.2022.06.205.
2 B. Sharma, A. Sharma and J.-S. Kim, *Sens. Actuators, B*, 2018, **262**, 758–770.
3 S. E. Hosseini and M. A. Wahid, *Renewable Sustainable Energy Rev.*, 2016, **57**, 850–866.
4 A. Zhong, A. Sun, B. Shen, H. Yu, Y. Zhou, Y. Liu, Y. Xie, J. Luo, D. Zhang and P. Fan, *Int. J. Hydrogen Energy*, 2022, **47**, 2050–2058.
5 J. A. Okolie, B. R. Patra, A. Mukherjee, S. Nanda, A. K. Dalai and J. A. Kozinski, *Int. J. Hydrogen Energy*, 2021, **46**, 8885–8905.
6 X. Bévenot, A. Trouillet, C. Veillas, H. Gagnaire and M. Clément, *Sens. Actuators, B*, 2000, **67**, 57–67.
7 D. Berndt, J. Muggli, F. Wittwer, C. Langer, S. Heinrich, T. Knittel and R. Schreiner, *Sens. Actuators, A*, 2020, **305**, 111670.
8 X. Meng, M. Bi, Q. Xiao and W. Gao, *Sens. Actuators, B*, 2022, **359**, 131612.
9 X.-T. Yin, S.-S. Wu, D. Dastan, S. Nie, Y. Liu, Z.-G. Li, Y.-W. Zhou, J. Li, A. Faik, K. Shan, Z. Shi, M. A. Tarighat and X.-G. Ma, *Surf. Interfaces*, 2021, **25**, 101190.

10 S. Zhu, Q. Tian, G. Wu, W. Bian, N. Sun, X. Wang, C. Li, Y. Zhang, H. Dou, C. Gong, X. Dong, J. Sun, Y. An, Q. Jing and B. Liu, *Int. J. Hydrogen Energy*, 2022, **47**, 17821–17834.
11 N. Van Duy, N. X. Thai, T. M. Ngoc, D. Thi Thanh Le, C. M. Hung, H. Nguyen, M. Tonezzer, N. Van Hieu and N. D. Hoa, *Sens. Actuators, B*, 2022, **351**, 130979.
12 T. Sahoo and P. Kale, *Adv. Mater. Interfaces*, 2021, **8**, 2100649.
13 G. Korotcenkov, S. D. Han and J. R. Stetter, *Chem. Rev.*, 2009, **109**, 1402–1433.
14 J. Ou, M. H. Yaacob, J. L. Campbell, K. Kalantar-zadeh and W. Wlodarski, *Procedia Eng.*, 2010, **5**, 1204–1207.
15 I. Constantinoiu and C. Viespe, *Nanomaterials*, 2020, **10**, 760.
16 S. S. Kalanur, Y.-A. Lee and H. Seo, *RSC Adv.*, 2015, **5**, 9028–9034.
17 Y. K. Kim, S. H. Hwang, S. M. Jeong, K. Y. Son and S. K. Lim, *Talanta*, 2018, **188**, 356–364.
18 Y. Shi, H. Xu, T. Liu, S. Zeb, Y. Nie, Y. Zhao, C. Qin and X. Jiang, *Adv. Mater.*, 2021, **2**, 1530–1569.
19 A. Mirzaei, S. G. Leonardi and G. Neri, *Ceram. Int.*, 2016, **42**, 15119–15141.
20 A. Mirzaei and G. Neri, *Sens. Actuators, B*, 2016, **237**, 749–775.
21 A. Mirzaei, S. S. Kim and H. W. Kim, *J. Hazard. Mater.*, 2018, **357**, 314–331.
22 A. Mirzaei, J.-H. Kim, H. W. Kim and S. S. Kim, *J. Mater. Chem. C*, 2018, **6**, 4342–4370.
23 P ist der Anmelder, *Germany Pat.*, DE2016388A1, 1971.
24 H.-J. Kim and J.-H. Lee, *Sens. Actuators, B*, 2014, **192**, 607–627.
25 S. Das and V. Jayaraman, *Prog. Mater. Sci.*, 2014, **66**, 112–255.
26 N. Yamazoe, *Catal. Surv. Asia*, 2003, **7**, 63–75.
27 N. Yamazoe and K. Shimanoe, in *Science and Technology of Chemiresistor Gas Sensors*, Nova Science Publishers, Inc., 2007, pp. 1–31.
28 Y. Masuda, *Sens. Actuators, B*, 2022, **364**, 131876.
29 S. Sub Kim, H. Gil Na, H. Woo Kim, V. Kulish and P. Wu, *Sci. Rep.*, 2015, **5**, 10723.
30 Y. J. Kwon, S. Y. Kang, P. Wu, Y. Peng, S. S. Kim and H. W. Kim, *ACS Appl. Mater. Interfaces*, 2016, **8**, 13646–13658.
31 D. Meng, D. Liu, G. Wang, Y. Shen, X. San, M. Li and F. Meng, *Sens. Actuators, B*, 2018, **273**, 418–428.
32 X. Lian, Y. Li, J. Zhu, Y. Zou, D. An and Q. Wang, *Mater. Sci. Semicond. Process.*, 2019, **101**, 198–205.
33 G. Li, Z. Cheng, Q. Xiang, L. Yan, X. Wang and J. Xu, *Sens. Actuators, B*, 2019, **283**, 590–601.
34 Y. Luo, C. Zhang, B. Zheng, X. Geng and M. Debliquy, *Int. J. Hydrogen Energy*, 2017, **42**, 20386–20397.
35 T. Xu, M. P. Zach, Z. L. Xiao, D. Rosenmann, U. Welp, W. K. Kwok and G. W. Crabtree, *Appl. Phys. Lett.*, 2005, **86**, 203104.
36 A. Mirzaei, H. R. Yousefi, F. Falsafi, M. Bonyani, J.-H. Lee, J.-H. Kim, H. W. Kim and S. S. Kim, *Int. J. Hydrogen Energy*, 2019, **44**, 20552–20571.
37 N. Yamazoe, *Sens. Actuators, B*, 1991, **5**, 7–19.
38 O. Lupan, V. Postica, F. Labat, I. Ciofini, T. Pauporté and R. Adelung, *Sens. Actuators, B*, 2018, **254**, 1259–1270.
39 M. Weber, J. H. Kim, J. H. Lee, J. Y. Kim, I. Iatsunskyi, E. Coy, M. Drobek, A. Julbe, M. Bechelany and S. S. Kim, *ACS Appl. Mater. Interfaces*, 2018, **10**, 34765–34773.
40 C. T. Campbell, *Surf. Sci. Rep.*, 1997, **27**, 1–111.
41 S. J. Tauster, S. C. Fung and R. L. Garten, *J. Am. Chem. Soc.*, 2002, **100**, 170–175.
42 L. Assaud, N. Brazeau, M. K. S. Barr, M. Hanbücken, S. Ntais, E. A. Baranova and L. Santinacci, *ACS Appl. Mater. Interfaces*, 2015, **7**, 24533–24542.
43 M. K. S. Barr, L. Assaud, N. Brazeau, M. Hanbücken, S. Ntais, L. Santinacci and E. A. Baranova, *J. Phys. Chem. C*, 2017, **121**, 17727–17736.
44 S. Sayegh, J.-H. Lee, D.-H. Yang, M. Weber, I. Iatsunskyi, E. Coy, A. Razzouk, S. S. Kim and M. Bechelany, *Sens. Actuators, B*, 2021, **344**, 130302.
45 M. Weber, J. Y. Kim, J. H. Lee, J. H. Kim, I. Iatsunskyi, E. Coy, P. Miele, M. Bechelany and S. S. Kim, *J. Mater. Chem. A*, 2019, **7**, 8107–8116.
46 X. Xiao, H. Wang, W. Bao, P. Urbankowski, L. Yang, Y. Yang, K. Maleski, L. Cui, S. J. L. Billinge, G. Wang and Y. Gogotsi, *Adv. Mater.*, 2019, **31**, e1902393.
47 H. C. M. Knoops, L. Baggetto, E. Langereis, M. C. M. van de Sanden, J. H. Klootwijk, F. Roozeboom, R. A. H. Niessen, P. H. L. Notten and W. M. M. Kessels, *J. Electrochem. Soc.*, 2008, **155**, G287–G294.
48 M.-D. Cheng, T. Luoh, C.-T. Su, T.-H. Yang, K.-C. Chen and C.-Y. Lu, *Thin Solid Films*, 2010, **518**, 2285–2289.
49 A. Shearrow, G. Koolstra, S. J. Whiteley, N. Earnest, P. S. Barry, F. J. Heremans, D. D. Awschalom, E. Shirokoff and D. I. Schuster, *Appl. Phys. Lett.*, 2018, **113**, 212601.
50 J.-Z. Kong, P. Xu, Y.-Q. Cao, A.-D. Li, Q.-Z. Wang and F. Zhou, *Surf. Coat. Technol.*, 2020, **381**, 125108.
51 Z. Pan, Y. Xiao, Z. Fu, G. Zhan, S. Wu, C. Xiao, G. Hu and Z. Wei, *J. Mater. Chem. A*, 2014, **2**, 13966–13975.
52 S. Liu, W. Qi, S. Adimi, H. Guo, B. Weng, J. P. Attfield and M. Yang, *ACS Appl. Mater. Interfaces*, 2021, **13**, 7238–7247.
53 A. Kolmakov, D. O. Klenov, Y. Lilach, S. Stemmer and M. Moskovits, *Nano Lett.*, 2005, **5**, 667–673.
54 X. Wang, N. Aroonyadet, Y. Zhang, M. Mecklenburg, X. Fang, H. Chen, E. Goo and C. Zhou, *Nano Lett.*, 2014, **14**, 3014–3022.
55 M. Leskelä and M. Ritala, *Thin Solid Films*, 2002, **409**, 138–146.
56 R. W. Johnson, A. Hultqvist and S. F. Bent, *Mater. Today*, 2014, **17**, 236–246.
57 A. S. Asundi, J. A. Raiford and S. F. Bent, *ACS Energy Lett.*, 2019, **4**, 908–925.
58 C. Marichy, M. Bechelany and N. Pinna, *Adv. Mater.*, 2012, **24**, 1017–1032.
59 C. H. Ahn, S. G. Cho, H. J. Lee, K. H. Park and S. H. Jeong, *Met. Mater. Int.*, 2001, **7**, 621–625.
60 J.-S. Min, Y.-W. Son, W.-G. Kang, S.-S. Chun and S.-W. Kang, *Jpn. J. Appl. Phys.*, 1998, **37**, 4999–5004.
61 J.-W. Lim, J.-S. Park and S.-W. Kang, *J. Appl. Phys.*, 2000, **87**, 4632–4634.
62 L. Assaud, K. Pitzschel, M. Hanbücken and L. Santinacci, *ECS J. Solid State Sci. Technol.*, 2014, **3**, P253–P258.

 

63 C. Badie, H. Tissot, B. Sciacca, M. K. Barr, J. Bachmann, C. Vallée, G. Gautier, T. Defforge, V. Astie, J.-M. Decams, M. Bechelany and L. Santinacci, *J. Vac. Sci. Technol., A*, 2022, **41**, 032401.

64 L. Assaud, E. Monyoncho, K. Pitzschel, A. Allagui, M. Petit, M. Hanbücken, E. A. Baranova and L. Santinacci, *Beilstein J. Nanotechnol.*, 2014, **5**, 162–172.

65 M. Weber, C. Lamboux, B. Navarra, P. Miele, S. Zanna, M. E. Dufond, L. Santinacci and M. Bechelany, *Nanomaterials*, 2018, **8**.

66 A. J. Mackus, M. J. Weber, N. F. Thissen, D. Garcia-Alonso, R. H. Vervuurt, S. Assali, A. A. Bol, M. A. Verheijen and W. M. Kessels, *Nanotechnology*, 2016, **27**, 034001.

67 F. S. Fedorov, D. Settipani, M. E. Melandsø Buan, J. Sainio, F. S. M. Ali, D. Ilatovskii, T. Kallio and A. G. Nasibulin, *ChemElectroChem*, 2020, **7**, 2651–2659.

68 J. W. Elam, A. Zinovev, C. Y. Han, H. H. Wang, U. Welp, J. N. Hryn and M. J. Pellin, *Thin Solid Films*, 2006, **515**, 1664–1673.

69 P. C. Stair, *J. Chem. Phys.*, 2008, **128**, 182507.

70 D. N. Goldstein and S. M. George, *Thin Solid Films*, 2011, **519**, 5339–5347.

71 H. Feng, J. A. Libera, P. C. Stair, J. T. Miller and J. W. Elam, *ACS Catal.*, 2011, **1**, 665–673.

72 M. Weber, P. Collot, H. El Gaddari, S. Tingry, M. Bechelany and Y. Holade, *ChemElectroChem*, 2018, **5**, 743–747.

73 T. L. H. Doan, J.-Y. Kim, J.-H. Lee, L. H. T. Nguyen, Y. T. Dang, K.-B. T. Bui, A. T. T. Pham, A. Mirzaei, T. B. Phan and S. S. Kim, *Sens. Actuators, B*, 2021, **348**, 130684.

74 T. L. H. Doan, J.-Y. Kim, J.-H. Lee, L. H. T. Nguyen, H. T. T. Nguyen, A. T. T. Pham, T. B. Nguyen Le, A. Mirzaei, T. B. Phan and S. S. Kim, *Sens. Actuators, B*, 2021, **349**, 130741.

75 D. B. Williams and C. B. Carter, *Transmission Electron Microscopy*, Springer, New York, NY, 2009.

76 D. Wanger, W. M. Riggs, L. E. Davis and J. F. Moulder, *Handbook of X-Ray Photoelectron Spectroscopy*, Perkin-Elmer Corp., Physical Electronics Division, Eden Prairie, Minnesota, USA, 1979.

77 N. C. Saha and H. G. Tompkins, *J. Appl. Phys.*, 1992, **72**, 3072–3079.

78 M. A. Al-Ghouti and D. A. Da'ana, *J. Hazard. Mater.*, 2020, **393**, 122383.

79 M. S. Choi, M. Y. Kim, A. Mirzaei, H.-S. Kim, S.-i. Kim, S.-H. Baek, D. Won Chun, C. Jin and K. Hyoung Lee, *Appl. Surf. Sci.*, 2021, **568**, 150910.

80 V. Brynzari, G. Korotchenkov and S. Dmitriev, *Sens. Actuators, B*, 1999, **61**, 143–153.

81 V. T. Nguyen, V. C. Nguyen, V. D. Nguyen, S. H. Hoang, N. Hugo, D. H. Nguyen and V. H. Nguyen, *J. Hazard. Mater.*, 2016, **301**, 433–442.

82 J.-H. Kim, A. Mirzaei, H. W. Kim and S. S. Kim, *Sens. Actuators, B*, 2019, **285**, 358–367.

83 K. Nguyen, C. M. Hung, T. M. Ngoc, D. T. Thanh Le, D. H. Nguyen, D. Nguyen Van and H. Nguyen Van, *Sens. Actuators, B*, 2017, **253**, 156–163.

84 A. Umar, H. Y. Ammar, R. Kumar, T. Almas, A. A. Ibrahim, M. S. AlAssiri, M. Abaker and S. Baskoutas, *Int. J. Hydrogen Energy*, 2020, **45**, 26388–26401.

85 X. T. Yin, J. Li, Q. Wang, D. Dastan, Z. C. Shi, N. Alharbi, H. Garmestani, X. M. Tan, Y. Liu and X. G. Ma, *Langmuir*, 2021, **37**, 13548–13558.

86 P. G. Choi, N. Izu, N. Shirahata and Y. Masuda, *ACS Omega*, 2018, **3**, 14592–14596.

87 X. Zhang, J. Sun, K. Tang, H. Wang, T. Chen, K. Jiang, T. Zhou, H. Quan and R. Guo, *Microsyst. Nanoeng.*, 2022, **8**, 67.

88 E. Lee, Y. S. Yoon and D. J. Kim, *ACS Sens.*, 2018, **3**, 2045–2060.

89 G. Y. Chai, O. Lupan, E. V. Rusu, G. I. Stratan, V. V. Ursaki, V. Șontea, H. Khallaf and L. Chow, *Sens. Actuators, A*, 2012, **176**, 64–71.

90 Y. Zhang, J. Xu, Q. Xiang, H. Li, Q. Pan and P. Xu, *J. Phys. Chem. C*, 2009, **113**, 3430–3435.

91 Sunaina, K. K. Yadav, Ankush, S. K. Guchhait, K. Sood, S. K. Mehta, A. K. Ganguli and M. Jha, *Sep. Purif. Technol.*, 2020, **242**, 116835.

92 F. Fillot, T. Morel, S. Minoret, I. Matko, S. Maîtrejean, B. Guillaumot, B. Chenevier and T. Billon, *Microelectron. Eng.*, 2005, **82**, 248–253.

93 S. Dhall, M. Kumar, M. Bhatnagar and B. R. Mehta, *Int. J. Hydrogen Energy*, 2018, **43**, 17921–17927.

94 J.-H. Kim, A. Mirzaei, H. W. Kim and S. S. Kim, *Sens. Actuators, B*, 2019, **297**, 126693.